

# Crack propagation in anisotropic brittle materials: from a phase-field model to a shape optimization approach

Tim Suchan<sup>\*1</sup>, Chaitanya Kandekar<sup>1</sup>, Wolfgang E. Weber<sup>1</sup>, and Kathrin Welker<sup>2</sup>

<sup>1</sup>Professorship of Structural Analysis, HELMUT SCHMIDT University / University of the Federal Armed Forces Hamburg, Holstenhofweg 85, 22043 Hamburg, Germany

<sup>2</sup>Professorship of Mathematical Optimization, Technische Universität Bergakademie Freiberg, Akademiestraße 6, 09599 Freiberg, Germany

September 6, 2023

## Abstract

The phase-field method is based on the energy minimization principle which is a geometric method for modeling diffusive cracks that are popularly implemented with irreversibility based on GRIFFITH's criterion. This method requires a length-scale parameter that smooths the sharp discontinuity, which influences the diffuse band and results in mesh-sensitive fracture propagation results. Recently, a novel approach based on the optimization on RIEMANNIAN shape spaces has been proposed, where the crack path is realized by techniques from shape optimization. This approach requires the shape derivative, which is derived in a continuous sense and used for a gradient-based algorithm to minimize the energy of the system. Due to the continuous derivation of the shape derivative, this approach yields mesh-independent results. In this paper, the novel approach based on shape optimization is presented, followed by an assessment of the predicted crack path in anisotropic brittle material using numerical calculations from a phase-field model.

**Keywords:** shape optimization, phase-field method, GRIFFITH's criterion, anisotropic material, shape space

---

<sup>\*</sup>Corresponding author: suchan@hsu-hh.de

# 1 Introduction

Phase-field modelling is a widely used approach to solve various types of multi-physics phenomena, particularly in fracture problems, in both the physics and the mechanics community [7]. Application include mechanical engineering, civil engineering, hydraulic engineering [37] or aerospace engineering [22, 45, 46]. In general, the phase-field method is a technique which is used to model sharp interfaces with the help of a continuous scalar field variable, which facilitates the difference between multiple physical phases. In fracture mechanics applications, multiple phases are interpreted as solid (intact) or fully broken. Thus, the phase-field approach is used for modelling brittle fracture to predict crack initiation, propagation, merging, and branching. Due to its simplicity in implementation, this methodology has gained wide interest in the engineering community since 2008. The main driving force for these developments is the possibility to handle complex fracture phenomena within numerical methods in two and three dimensions. In recent years, several brittle fracture applications [4, 23, 27, 28, 35, 53, 61] and an extension to anisotropy [11, 39, 56] have been published. It was further developed also for isogeometric analysis [12] and the virtual element method (VEM) [1]. Applications for ductile fracture are also described in [3, 6]. Furthermore, the phase-field method is also applied in multi-physics problems such as corrosion [2, 32] and corrosion cracking [14, 15, 24]. These advances are mainly motivated by the capacity to handle complex fracture propagation in two- and three-dimensional numerical approaches. These investigations include a wide range of topics, including the modeling of 2D and 3D small and large strain deformations, variational formulations, multi-scale problems, mathematical analysis, various decompositions, and discretization approaches with numerous applications in science and engineering.

Shape optimization has seen frequent uses for medical [41], structural [31, 42, 54], fluid-mechanical [5, 51, 57], and acoustical applications [25, 48] but the usage of shape optimization for fracture problems is relatively new. Recently, a novel method for solving brittle isotropic fracture problems by using a shape optimization approach that minimizes the energy in the system by a part of gradient-based techniques has been proposed in [55]. In that publication, the fracture is described by a surface of the discretized domain, and therefore has sharp edges, in contrast to a phase-field approach. Other shape optimization algorithms exist, e. g., gradient-free approaches [8] or approaches based on second-order derivatives [20, 49, 50], but show other disadvantages regarding the number of partial differential equation (PDE) evaluations or existence of and analytical effort of calculating higher derivatives. Due to the novel nature of the approach, several challenges are still present also for a gradient-based approach: extension of the approach to different material models, the implementation of the irreversibility of the fracture, and the computation of the deformation of the computational domain from the derivative of the energy with respect to the shape. In this manuscript, we aim to extend the gradient-based approach for brittle fracture in [55] to anisotropic material behavior and establish a compar-

ison between this approach and the previously-mentioned phase-field method. The fracture response of the isotropic and anisotropic elastic material is analyzed in two boundary value problems to illustrate the shape optimization approach in applications for both isotropic and anisotropic material.

The paper is organized as follows: Section 2 outlines the brittle fracture modelling and the fundamentals of both phase-field and shape optimization methods, to describe the underlying governing equations along with the necessary assumptions to simplify the problem. Section 3 includes a distinct structure of balance equations and their algorithmic implementation to calculate the crack propagation in anisotropic elastic medium using the finite element method (FEM) with shape optimization and phase-field approaches. Some numerical tests are carried out to substantiate our algorithmic developments and to test effects of anisotropy on the crack path in Section 4. Herein, the results of numerical tests are discussed. Finally, the summary and conclusions are provided in Section 5.

## 2 Modelling

In this section, we first outline a commonly-used model for brittle fracture in Section 2.1. Then, Section 2.2 presents how this general model can be adapted to a phase-field setting. Lastly, Section 2.3 describes the usage of the model for brittle fracture in a shape optimization algorithm.

### 2.1 Fracture model

As is well-known (cf., e.g., [17]), the stored energy due to linear elastic deformation of a domain  $\mathcal{B} \subset \mathbb{R}^2$  omitting any volume and surface loads can be computed as

$$E_{bulk} = \inf_{\mathbf{w} \in H^1(\mathcal{B}, \mathbb{R}^2)} \int_{\mathcal{B}} \Psi_0(\boldsymbol{\epsilon}(\mathbf{w})) \, d\mathbf{x},$$

where  $\Psi_0$  denotes the energy density function and is defined as

$$\Psi_0(\boldsymbol{\epsilon}(\mathbf{w})) = \frac{1}{2} \boldsymbol{\epsilon}(\mathbf{w}) : \mathbb{C} : \boldsymbol{\epsilon}(\mathbf{w}) = \frac{1}{2} \boldsymbol{\epsilon}^V(\mathbf{w}) \cdot \mathbf{C} \cdot \boldsymbol{\epsilon}^V(\mathbf{w}).$$

Herein, the strain tensor is defined as  $\boldsymbol{\epsilon}(\mathbf{w}) = \frac{1}{2} (\nabla \mathbf{w} + \nabla \mathbf{w}^\top)$ . The material stiffness tensor  $\mathbb{C}$  and  $\mathbf{C}$  describe the material behavior, and the stress is defined as  $\boldsymbol{\sigma}(\mathbf{w}) = \mathbb{C} : \boldsymbol{\epsilon}(\mathbf{w})$  and  $\boldsymbol{\sigma}^V(\mathbf{w}) = \mathbf{C} \cdot \boldsymbol{\epsilon}^V(\mathbf{w})$ , respectively. Here, in view of the implementation of anisotropy of the material stiffness, strain, and stress tensor have been expressed in VOIGT notation<sup>1</sup>. In case of isotropic behavior,

<sup>1</sup>By using the symmetry of the tensors, the VOIGT notation [58] describes canonical isomorphisms

$$\begin{aligned} \mathbb{R}_{sym}^{2 \times 2 \times 2 \times 2} &\rightarrow \mathbb{R}^{3 \times 3}, \mathbb{C} \mapsto \mathbf{C}, \\ \mathbb{R}_{sym}^{2 \times 2} &\rightarrow \mathbb{R}^3, \boldsymbol{\epsilon} \mapsto \boldsymbol{\epsilon}^V, \text{ and} \\ \mathbb{R}_{sym}^{2 \times 2} &\rightarrow \mathbb{R}^3, \boldsymbol{\sigma} \mapsto \boldsymbol{\sigma}^V. \end{aligned}$$

$\mathbf{C} = \mathbf{C}_0$ . For anisotropic materials,  $\mathbf{C}(\theta) = \mathbf{P}(\theta)^\top \mathbf{C}^{ref} \mathbf{P}(\theta)$  with a rotation matrix defined for a rotation angle  $\theta \in [0, \pi]$ , cf. [29, 40], as

$$\mathbf{P}(\theta) = \begin{pmatrix} \cos^2(\theta) & \sin^2(\theta) & -2 \cos(\theta) \sin(\theta) \\ \sin^2(\theta) & \cos^2(\theta) & 2 \cos(\theta) \sin(\theta) \\ \cos(\theta) \sin(\theta) & -\cos(\theta) \sin(\theta) & \cos^2(\theta) - \sin^2(\theta) \end{pmatrix}.$$

The strong form of linear elasticity can be determined from  $E_{bulk}$  in absence of volume loads and tractions and reads (cf., e.g., [60])

$$\begin{aligned} \operatorname{div}(\boldsymbol{\sigma}(\mathbf{w})) &= \mathbf{0} \text{ in } \mathcal{B}, \\ \mathbf{w} &= \bar{\mathbf{w}} \text{ on } \partial\mathcal{B}_D, \\ \boldsymbol{\sigma}(\mathbf{w})\mathbf{n} &= \mathbf{0} \text{ on } \partial\mathcal{B} \setminus \partial\mathcal{B}_D. \end{aligned} \tag{1}$$

The part of the boundary  $\partial\mathcal{B}_D \subset \partial\mathcal{B}$ ,  $\partial\mathcal{B}_D \neq \emptyset$  describes the part where DIRICHLET boundary conditions are imposed<sup>2</sup>.

In order to model the fracture behavior, GRIFFITH has described a failure criterion based on the fracture toughness or GRIFFITH's criterion  $G_c > 0$  in [19]. In the following, it is assumed that the crack surface  $\Gamma$  is smooth enough such that the fracture energy of  $\Gamma$  can be described by

$$E_{frac} = \int_{\Gamma} G_c \, ds \tag{2}$$

as proposed in [17]. Therefore, the total energy of the system is given by

$$E_{total} = E_{bulk} + E_{frac}.$$

In view of the shape optimization approach, in some parts of the manuscript the total energy  $E_{total}$  is also denoted by  $J$ .

## 2.2 Adaption of the fracture model to the phase-field setting

For the phase-field problem, a sharp-crack surface topology  $\Gamma$  is regularized by the crack surface functional  $\Gamma_{l_s}$  using scalar field variable  $d: \mathcal{B} \rightarrow [0, 1]$ ,  $\mathbf{x} \mapsto d(\mathbf{x})$ , which is introduced to indicate a crack if  $d(\cdot) = 1$  and solid (intact) material if  $d(\cdot) = 0$  along with the smooth transition among them, cf. [35]. The crack surface functional  $\Gamma_{l_s}$  can be written as

$$\Gamma_{l_s}(d) = \int_{\mathcal{B}} \gamma_l(d, \nabla d) \, dV \quad \text{with} \quad \gamma_l(d, \nabla d) = \frac{1}{2l_s} d^2 + \frac{l_s}{2} \|\nabla d\|^2,$$

---

<sup>2</sup>In the numerical experiments in Section 4 DIRICHLET boundary conditions are only imposed in  $x$  or in  $y$  direction to avoid the introduction of additional stresses. Only one point of the domain is constrained in both  $x$  and  $y$  direction. To avoid an overcomplicated and confusing notation we use the description in (1) in any case.

where  $\gamma_l$  is the crack surface density function per unit volume of the solid and  $l_s > 0$  is the length scale parameter that governs the regularization. The free energy required to generate the crack is taken from the classical definition using GRIFFITH's failure criteria as

$$\Psi_{frac} = G_c \left( \frac{1}{2l_s} d^2 + \frac{l_s}{2} |\nabla d|^2 \right).$$

To describe a purely geometric approach to phase-field fracture, the regularized crack phase-field  $d$  is obtained by a minimization principle of diffusive crack topology

$$d = \arg \inf_{d \in \mathcal{D}_\Gamma} \Gamma_{l_s}(d)$$

with  $\mathcal{D}_\Gamma := \{d: d(\Gamma) = 1\}$ . The EULER equations of the above variational principle are

$$\begin{aligned} d - l_s^2 \Delta d &= 0 \text{ in } \mathcal{B}, \\ d &= 1 \text{ on } \Gamma, \\ \nabla d \cdot \mathbf{n} &= 0 \text{ on } \partial\mathcal{B} \setminus \Gamma, \end{aligned}$$

where  $\mathbf{n}$  is the outward normal on  $\partial\mathcal{B}$ , cf. [36]. The local equation for the evolution of the crack phase-field in the domain  $\mathcal{B}$  can be derived assuming global irreversibility condition of the crack evolution (cf. [36]) as

$$\frac{G_c}{l_s} (d - l_s^2 \Delta d) - 2(1 - d) \Psi_0^+(\boldsymbol{\epsilon}(\mathbf{w})) = 0,$$

where the effective crack-driving force  $\Psi_0^+(\boldsymbol{\epsilon}(\mathbf{w}))$  is based on strain splitting<sup>3</sup>. However, in line with the hybrid phase-field formulation from [7] the total energy is degraded fully in order to keep the computational cost comparable to the isotropic case. The degradation function is given as

$$g(d) = (1 - d)^2 + k,$$

where  $k > 0$  is an algorithmic constant. Similar to [24] we choose  $k = 10^{-7}$  for this paper. The parameter  $k$  circumvents the full degradation of the free energy and leaves an artificial elastic rest energy density of  $k\Psi_0(\boldsymbol{\epsilon}(\mathbf{w}))$  when fully broken.

### 2.3 Adaption of the fracture model to the shape optimization setting

In contrast to the phase-field approach outlined in Section 2.2, an alternative approach to simulate fracture propagation has been proposed in [55] and is

<sup>3</sup>For isotropic materials, the term  $\Psi_0^+(\boldsymbol{\epsilon}(\mathbf{w}))$  is defined as  $\frac{K}{2} \langle \text{tr}(\boldsymbol{\epsilon}(\mathbf{w})) \rangle_+^2 + \mu \langle \boldsymbol{\epsilon}^{dev}(\mathbf{w}) : \boldsymbol{\epsilon}^{dev}(\mathbf{w}) \rangle$ , where  $K > 0$  and  $\mu > 0$  denote bulk modulus and shear modulus, respectively,  $\langle \cdot \rangle_+$  is the MACAULAY bracket, and  $\boldsymbol{\epsilon}^{dev}(\mathbf{w})$  represents the deviatoric part of the strain tensor. For anisotropy, this is not usable—therefore, strain decomposition is not used.

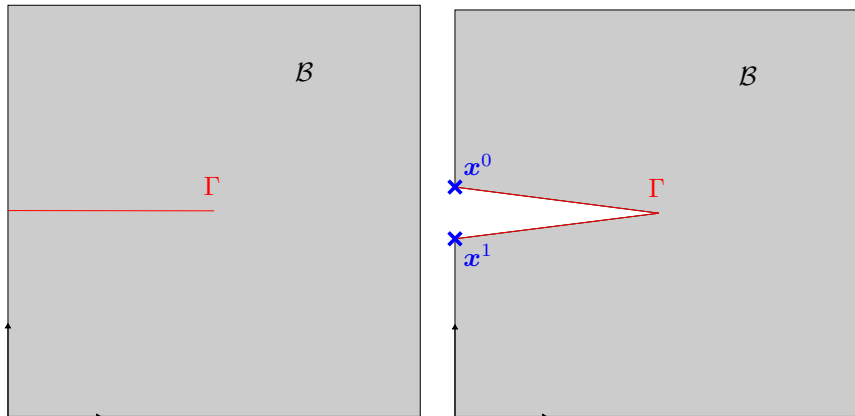


Figure 1: Replacement of an infinitesimally thin fracture for the single-edge notch test (left) by an open curve as part of the boundary of  $\mathcal{B}$  (right).

sketched in what follows. It is also based on the energy formulation but not using the phase-field  $d$ . Here, the problem is interpreted as a shape optimization problem with the goal of minimizing the energy  $E_{total}$  constrained by a partial differential equation for the displacement  $\mathbf{w} = (w_x, w_y)^\top \in H^1(\mathcal{B}, \mathbb{R}^2)$ . In our setting, the minimization of the energy is constrained by linear elasticity. The corresponding problem can be formulated as

$$\min_{\Gamma} \int_{\mathcal{B}} \frac{1}{2} \boldsymbol{\epsilon}^V(\mathbf{w}) \cdot \mathbf{C} \cdot \boldsymbol{\epsilon}^V(\mathbf{w}) \, d\mathbf{x} + \int_{\Gamma} G_c \, ds + \nu \int_{\mathcal{B}} 1 \, d\mathbf{x} \quad (4a)$$

$$\text{s.t.} \quad \int_{\mathcal{B}} (\mathbf{C} \cdot \boldsymbol{\epsilon}^V(\mathbf{w})) \cdot \boldsymbol{\epsilon}^V(\tilde{\mathbf{w}}) \, d\mathbf{x} = 0 \quad \forall \tilde{\mathbf{w}} \in H^1(\mathcal{B}, \mathbb{R}^2) \quad (4b)$$

$$+ \text{appropriate boundary conditions.} \quad (4c)$$

The last term in (4a) describes a volume regularization term with  $\nu > 0$  in order to incentivize that the fracture remains approximately one-dimensional. We embed the optimization into a theoretical framework in order to benefit from optimization algorithms with established convergence properties.

In (4a), the shape  $\Gamma$  representing the fracture is not specified so far. Multiple options are available for the description of a shape—among these are landmark vectors [26], plane curves [34, 33, 38], boundary contours of objects [30, 47], multiphase objects [59], characteristic functions of measurable sets [62] or morphologies of images [16]. We focus on the description of plane curves in this publication. For this, it has been motivated in [55] to replace the fracture by a curve towards the fracture tip and a curve back to the outer boundary in case the fracture has zero thickness. This setting is encountered, e.g., for the single-edge notch test, and is sketched in Figure 1. For an easier comparison we also use this mesh for the phase-field simulations. Ideally, the space of all admissible shapes, the so-called shape space, would allow a vector space structure; this would make the formulation of algorithms relatively simple. How-

ever, many commonly used shape spaces do not provide this—among them is both, the shape space  $B_e([0, 1], \mathbb{R}^2)$  (cf. [34]) containing all smooth embeddings of the unit interval into  $\mathbb{R}^2$  excluding reparametrizations, as well as the shape space  $M_s(B_e([0, 1], \mathbb{R}^2)^N)$  from [43], where  $s$  denotes the overall number of cracks. Both spaces admit an infinite dimensional RIEMANNIAN manifold structure, which can then be exploited to formulate gradient descent algorithms. An overview for shape optimization based on optimization on RIEMANNIAN manifolds with a focus on engineering applications can be found in [44]. This concept has been extended in [18], where the space  $M_s^c$  has been introduced that can be used to describe multiple piecewise smooth closed curves. In the present publication, we require a shape space that allows multiple piecewise smooth open curves. Since the shape space  $B_e([0, 1], \mathbb{R}^2)$  does not allow the development of kinks in the shapes we adapt the definition of  $M_s^c$  to obtain a space that allows  $s \in \mathbb{N}$  piecewise smooth open curves<sup>4</sup> starting at point  $\mathbf{x}_i^0$  and ending at point  $\mathbf{x}_i^1$ , where  $i$  indicates the respective crack:

$$\begin{aligned}
M_s^o &:= \{ \mathbf{\Gamma} = (\Gamma_1, \dots, \Gamma_s) \in M_s(B_e([0, 1], \mathbb{R}^2)^N) : \\
&\quad \Gamma_i : [0, 1] \rightarrow \mathbb{R}^2 \text{ injective with } \Gamma_i(0) = \tilde{\Gamma}_{k_i}(0) = \mathbf{x}_i^0, \\
&\quad \Gamma_i(1) = \tilde{\Gamma}_{k_i+n_i-1}(1) = \mathbf{x}_i^1 \text{ and } \tilde{\Gamma}_{k_i+h}(1) = \tilde{\Gamma}_{k_i+h+1}(0) \forall h = 0, \dots, n_i - 2 \},
\end{aligned} \tag{5}$$

where

$$\begin{aligned}
&M_s(B_e([0, 1], \mathbb{R}^2)^N) \\
&:= \left\{ \mathbf{\Gamma} = (\Gamma_1, \dots, \Gamma_s) : \Gamma_i \in \prod_{l=k_i}^{k_i+n_i-1} B_e([0, 1], \mathbb{R}^2) \forall i = 1, \dots, s, \right. \\
&\quad \left. \sum_{i=1}^s n_i = N, k_1 = 1, k_{i+1} = k_i + n_i \forall i = 1, \dots, s - 1 \right\}
\end{aligned}$$

is the  $s$ -dimensional shape space on  $B_e([0, 1], \mathbb{R}^2)^N$  from [43]. For all  $i = 1, \dots, s$  the piecewise smooth curve  $\Gamma_i$  in (5) consists of  $n_i$  smooth curves  $\tilde{\Gamma}_{k_i+h}$ ,  $h = 0, \dots, n_i - 2$ . The start point of one smooth curve in (5) is connected to the end point of the previous smooth curve, i.e., the curve  $\tilde{\Gamma}_{k_i+h+1}$  starts at the point where the curve  $\tilde{\Gamma}_{k_i+h}$  ends. The start and end point of  $\Gamma_i$  in (5) is defined as  $\mathbf{x}_i^0$  and  $\mathbf{x}_i^1$ , respectively. A kink in the piecewise smooth curve  $\Gamma_i$  can then develop at these connecting points. In some applications, the fracture is defined by only one open curve. In this case, the definition (5) simplifies to

$$\begin{aligned}
M_1^o &:= \{ \Gamma \in M_1(B_e([0, 1], \mathbb{R}^2)^N) : \\
&\quad \Gamma : [0, 1] \rightarrow \mathbb{R}^2 \text{ injective with } \Gamma(0) = \tilde{\Gamma}_1(0) = \mathbf{x}^0, \Gamma(1) = \tilde{\Gamma}_N(1) = \mathbf{x}^1 \text{ and} \\
&\quad \tilde{\Gamma}_h(1) = \tilde{\Gamma}_{h+1}(0) \forall h = 1, \dots, N - 1 \}.
\end{aligned}$$

---

<sup>4</sup>We use the superscript “o” for *open* in contrast to “c” for *closed* curves in this paper.

In order to establish a measure of distance between two different elements of  $M_s^o$  and to determine how one element is changed to another, a RIEMANNIAN metric on the shape space is required. The STEKLOV-POINCARÉ metric (cf. [51, 52]) is used in this publication because of its advantageous properties regarding the quality of the computational domain discretization. Due to the usage of the STEKLOV-POINCARÉ metric, we obtain a vector field  $\mathbf{V}: \mathcal{B} \rightarrow \mathbb{R}^2$  in an appropriate HILBERT space  $\mathcal{V}$  by solving the so-called deformation equation

$$a(\mathbf{V}, \mathbf{W}) = dJ(\Gamma)[\mathbf{W}] \quad \forall \mathbf{W} \in \mathcal{V} \quad (6)$$

with a symmetric and coercive bilinear form  $a: \mathcal{V} \times \mathcal{V} \rightarrow \mathbb{R}$  and the shape derivative  $dJ$  [51, Eq. (4.4)]. Please note that  $J$  equals the total energy  $E_{total}$  according to Section 2.1. The resulting vector field  $\mathbf{V}$  can then be used to update the domain as

$$\mathcal{B}_\tau = \{\mathbf{x} \in \mathcal{B}: \mathbf{x} + \tau \mathbf{V}(\mathbf{x})\}$$

with  $\tau \geq 0$ . The update of the curve  $\Gamma \subset \mathcal{B}$  is, accordingly,

$$\Gamma_\tau = \{\mathbf{x} \in \Gamma: \mathbf{x} + \tau \mathbf{V}(\mathbf{x})|_\Gamma\}.$$

The shape derivative of  $J$  at  $\Gamma$  in direction  $\mathbf{W}$  denoted by  $dJ(\Gamma)[\mathbf{W}]$  describes the change in energy due to the change of  $\Gamma$  (and  $\mathcal{B}$ , respectively) and is defined as

$$dJ(\Gamma)[\mathbf{W}] = \lim_{\tau \rightarrow 0^+} \frac{J(\Gamma_\tau) - J(\Gamma)}{\tau}$$

if it exists and is linear and continuous in  $\mathbf{W}$ . As described in [55], the shape derivative for our problem can be calculated with a material derivative approach [10] as

$$\begin{aligned} dJ(\Gamma)[\mathbf{W}] = & \int_{\mathcal{B}} -\frac{1}{2} \left( \nabla \mathbf{w} \nabla \mathbf{W} + (\nabla \mathbf{w} \nabla \mathbf{W})^\top \right) : \boldsymbol{\sigma}(\mathbf{w}) + \operatorname{div}(\mathbf{W}) \cdot \left( \frac{1}{2} \boldsymbol{\sigma}(\mathbf{w}) : \boldsymbol{\epsilon}(\mathbf{w}) \right) d\mathbf{x} \\ & + \frac{1}{2} \int_{\Gamma} G_c \kappa \mathbf{W}^\top \mathbf{n} ds - \int_{\Gamma} \nu \mathbf{W}^\top \mathbf{n} ds \end{aligned} \quad (7)$$

with  $\kappa$  as the curvature of  $\Gamma$ . The bilinear form  $a(\mathbf{V}, \mathbf{W})$  in (6) can be chosen arbitrarily and (6) is solely used to obtain the vector field  $\mathbf{V}$ . Common choices include the POISSON equation or the bilinear form of linear elasticity. Similar to [55] we use the bilinear form of linear elasticity. Solving for  $\mathbf{V}$  does not replace the linear elasticity equation to obtain  $\mathbf{w}$  but instead is an additional step to obtain the gradient. The problem to obtain for  $\mathbf{V} \in \mathcal{V}$  therefore reads

$$\underbrace{\int_{\mathcal{B}} \left( \tilde{\mathbb{C}} : \boldsymbol{\epsilon}(\mathbf{V}) \right) : \boldsymbol{\epsilon}(\mathbf{W}) d\mathbf{x}}_{a(\mathbf{V}, \mathbf{W})} = dJ(\Gamma)[\mathbf{W}] \quad \forall \mathbf{W} \in \mathcal{V}. \quad (8)$$



Following [51, 52] we choose the second LAMÉ parameter in  $\tilde{\mathbb{C}}$  to obtain  $\mathbf{V}$  as  $\tilde{\mu} = 5$  on  $\Gamma$  and  $\tilde{\mu} = 1$  on  $\partial\mathcal{B} \setminus \Gamma$  and perform an extension to obtain intermediate values inside of  $\mathcal{B}$ . The first LAMÉ parameter is chosen as  $\tilde{\lambda} = 10$  everywhere. These values are unrelated to the material parameters in the balance of linear momentum to obtain  $\mathbf{w}$ . Solving (8) further requires appropriate boundary conditions. Since only deformations of  $\Gamma$  should affect the objective functional that is to be minimized, an appropriate choice is to not allow deformations of  $\partial\mathcal{B} \setminus \Gamma$ , which yields a homogenous DIRICHLET boundary condition on  $\partial\mathcal{B} \setminus \Gamma$ . We further impose a homogenous DIRICHLET boundary condition on the part of  $\Gamma$  that fulfills  $0 < x < 0.48$  since no fracture growth can be expected in this area, and a homogenous NEUMANN boundary condition on the rest of  $\Gamma$ , which we denote as  $\hat{\Gamma}$ . The previously mentioned HILBERT space  $\mathcal{V}$  therefore can be chosen as

$$\mathcal{V} := \left\{ \mathbf{V} \in H^1(\mathcal{B}, \mathbb{R}^2) : \mathbf{V} = \mathbf{0} \text{ on } \partial\mathcal{B} \setminus \hat{\Gamma} \right\}.$$

Using the approach described above the fracture irreversibility condition is not ensured. Thus, for low mechanical loads on the physical system the fracture would actually shrink, which is an unphysical behavior, since the fracture cannot heal itself after developing. Similar to [55], we project the resulting vector field  $\mathbf{V}$  from (8) onto the set

$$\left\{ \mathbf{V} \in H^1(\mathcal{B}, \mathbb{R}^2) : \mathbf{V}^\top \mathbf{N} \leq 0, \mathbf{V} = \mathbf{0} \text{ on } \partial\mathcal{B} \setminus \hat{\Gamma} \right\} \quad (9)$$

to ensure irreversibility, where  $\mathbf{N}$  describes the unit outward normal vector on  $\Gamma$  extended into the domain  $\mathcal{B}$ . This is performed by solving the Eikonal equation

$$\varepsilon \Delta \Phi(\mathbf{x}) + |\nabla \Phi(\mathbf{x})| = 1 \quad \text{in } \mathcal{B}, \quad \Phi(\mathbf{x}) = 0 \quad \text{on } \Gamma, \quad \frac{\partial \Phi(\mathbf{x})}{\partial \mathbf{n}} = 0 \quad \text{on } \partial\mathcal{B} \setminus \Gamma \quad (10)$$

stabilized by an  $\varepsilon = 2 \cdot 10^{-3}$ . The normal vector extended into the domain  $\mathcal{B}$  can then be determined as  $\mathbf{N} = \nabla \Phi(\mathbf{x})$ . The irreversibility is enforced by replacing any  $\mathbf{V} \in \mathcal{V}$  that violates  $\mathbf{V}^\top \mathbf{N} \leq 0$  with  $\mathbf{V} = \mathbf{0}$ . This equates to a projected gradient descent algorithm.

### 3 Numerical implementation

In this section, numerical implementations are compared for both methods in order to get detailed insight about different approaches.

### 3.1 Implementation of the phase-field approach

As described in [21] the weak form of the bulk response in the EULERian setting is given as

$$\int_{\mathcal{B}} g(d) \boldsymbol{\sigma} : \nabla \delta \mathbf{w} \, d\mathbf{x} = 0 \quad \forall \delta \mathbf{w} \in H^1(\mathcal{B}, \mathbb{R}^2), \quad (11)$$

$$\int_{\mathcal{B}} \delta d \left( \frac{G_c}{l_s} + 2\mathcal{H} \right) d - 2\mathcal{H} \delta d + \nabla \delta d \cdot G_{cl_s} \nabla d \, d\mathbf{x} = 0 \quad \forall \delta d \in H^1(\mathcal{B}, \mathbb{R}). \quad (12)$$

The finite element method is used to discretize the domain  $\mathcal{B} = \bigcup_{e=1}^{N_e} \mathcal{B}^e$  with  $N_e$  as the number of elements. The residuum in the domain  $\mathcal{B}$  with the finite element discretization of the elements using linear shape functions with  $N_{(\cdot)}(\mathbf{x})$  as the shape functions and  $\mathbf{B}_{(\cdot)}(\mathbf{x})$  as their respective derivatives, are given as

$$\mathbf{r}_{\mathbf{w}} = \bigcup_{e=1}^{N_e} \int_{\mathcal{B}^e} g(d) \mathbf{B}_{\mathbf{w}}^\top \boldsymbol{\sigma}^V \, d\mathbf{x} = \mathbf{0}, \quad (13)$$

$$r_d = \bigcup_{e=1}^{N_e} \int_{\mathcal{B}^e} \mathbf{N}_d^\top \left[ \left( \frac{G_c}{l_s} + 2\mathcal{H} \right) d - 2\mathcal{H} \right] + \mathbf{B}_d^\top l_s^2 \nabla d \, d\mathbf{x} = 0. \quad (14)$$

This multi-field problem is solved using NEWTON-RAPHSON iterations in a staggered manner as depicted in Algorithm 1. Therein, a sequence of two linear subproblems for the successive update of the phase-field fracture and the displacement field is shown.

---

#### Algorithm 1 Numerical implementation for phase-field approach

---

- 1: **Input:** displacement increment  $\Delta \bar{\mathbf{w}} > \mathbf{0}$ , max. number of staggered iterations  $k_{\max} > 0$ , staggered tolerance  $tol_{stag} = 10^{-3}$
  - 2: **Initialization:**  $\mathbf{w} = \mathbf{0}$ ,  $d = 0$ ,  $\bar{\mathbf{w}} = \mathbf{0}$
  - 3: **while**  $\bar{\mathbf{w}} < \bar{\mathbf{w}}_{max}$  **do**
  - 4:     **Initialization:**  $k = 0$ ,  $(\mathbf{w}^0, d^0) = (\mathbf{w}, d)$
  - 5:     **while**  $k < k_{max}$  **do**
  - 6:         Solve (13) to obtain  $\mathbf{w}^k \in H^1(\mathcal{B}, \mathbb{R}^2)$  with  $d^{k-1}$  and  $\bar{\mathbf{w}}$
  - 7:         Solve (14) to obtain  $d^k \in H^1(\mathcal{B}, \mathbb{R})$  with  $\mathbf{w}^k$
  - 8:         Compute errornorm for obtained pair  $(\mathbf{w}^k, d^k)$
  - 9:         **if** errornorm  $\leq tol_{stag}$  **then**  $(\mathbf{w}, d) \leftarrow (\mathbf{w}^k, d^k)$  and **break**
  - 10:          $k \leftarrow k + 1$
  - 11:      $\bar{\mathbf{w}} \leftarrow \bar{\mathbf{w}} + \Delta \bar{\mathbf{w}}$
  - 12: **Output:** solution  $(\mathbf{w}, d)$ .
-

### 3.2 Implementation of the shape optimization approach

Similar to the phase-field approach, however without the phase-field variable  $d$ , the weak form for the displacement is given by linear elasticity (cf., e.g., [9]) as

$$\int_{\mathcal{B}} \boldsymbol{\sigma}(\mathbf{w}) : \nabla \delta \mathbf{w} \, d\mathbf{x} = 0 \quad \forall \delta \mathbf{w} \in H^1(\mathcal{B}, \mathbb{R}^2).$$

The finite element method with the same initial discretization and shape functions as in Section 2.2 is used to solve the PDE. Therefore, the residuum reads

$$\mathbf{r}_{\mathbf{w}} = \bigcup_{e=1}^{N_e} \int_{\mathcal{B}^e} \mathbf{B}_w^T \boldsymbol{\sigma}^V(\mathbf{w}) \, d\mathbf{x} = \mathbf{0} \quad (15)$$

and is solved by classical LU<sup>5</sup> factorization. Then, an additional linear PDE is solved to obtain the vector field from the shape derivative to update the computational mesh as described in (8). This yields the same weak form and discretization as for the displacement  $\mathbf{w}$  but with different material parameters. The specific choice of material parameters is described in Section 4. The Eikonal equation (10) is also solved using the same discretization with the standard NEWTON method, from which the extension of the normal vector into the domain is obtained by projecting  $\nabla \Phi$  to linear shape functions again. The projection onto the set (9) is performed by computing the scalar product of  $\mathbf{V}$  and  $\mathbf{N}$  at each degree of freedom (DOF) and if the scalar product is larger than zero, then  $\mathbf{V} = \mathbf{0}$  at this DOF. The projected vector field  $\mathbf{V}$  is then applied to  $\mathcal{B}$  using a constant step size of  $\tau = 10^{-2}$ . For our simulations, we choose a maximum number of iterations of  $k_{\max} = 5000$ , however this limit was not reached in any simulation shown in Section 4. The whole process is sketched in Algorithm 2.

## 4 Numerical examples

In this section, we show the numerical results from the Algorithms 1 and 2 for two different boundary value problems. In Section 4.1, we investigate the V-notch model as described in [13] under tension and compare boundary forces and fracture path between the two different approaches. Then, Section 4.2 demonstrates the numerical results for fracture propagation of the single-edge notch tension test with anisotropic material behavior.

### 4.1 Boundary Value Problem 1: V-notch – Isotropy

For this numerical experiment, we use the double V-notch plate with the geometric properties and computational mesh shown in Figure 2. The discretization of the model contains 13 434 triangular elements. The mesh is refined in the central region where the crack is expected to develop. The red lines denote

<sup>5</sup>‘LU’ is the abbreviation of ‘lower-upper.’

---

**Algorithm 2** Numerical implementation for shape optimization

---

- 1: **Input:** Initial domain  $\mathcal{B}^1 \subset \mathbb{R}^2$ , step size  $\tau > 0$ , max. number of iterations  $k_{\max} > 0$ , displacement increment  $\Delta \bar{\mathbf{w}} > \mathbf{0}$
  - 2: **Initialization:**  $\bar{\mathbf{w}} = \mathbf{0}$
  - 3: **while**  $\bar{\mathbf{w}} < \bar{\mathbf{w}}_{\max}$  **do**
  - 4:   **Initialization:**  $k := 1$
  - 5:   **while**  $k < k_{\max}$  **do**
  - 6:     Solve (15) to obtain  $\mathbf{w} \in H^1(\mathcal{B}, \mathbb{R}^2)$  with  $\bar{\mathbf{w}}$
  - 7:     Compute  $J(\mathcal{B}^k)$
  - 8:     Generate vector field  $\mathbf{V}$  by solving (8)
  - 9:     Project  $\mathbf{V}$  onto (9)
  - 10:      $\mathcal{B}^{k+1} \leftarrow \{\mathbf{x} \in \mathcal{B}^k : \mathbf{x} + \tau \mathbf{V}(\mathbf{x})\}$
  - 11:     **if**  $J(\mathcal{B}^{k+1}) \geq J(\mathcal{B}^k)$  **then break**
  - 12:      $k \leftarrow k + 1$
  - 13:    $\bar{\mathbf{w}} \leftarrow \bar{\mathbf{w}} + \Delta \bar{\mathbf{w}}$
- 

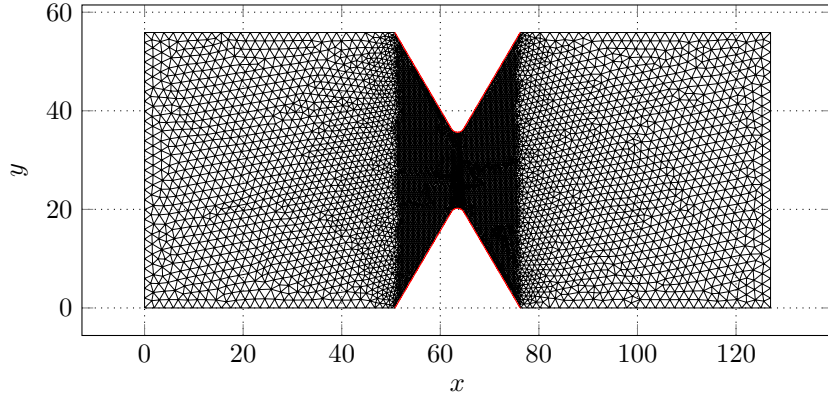


Figure 2: Mesh for V-notch: Nodes - 6900, Elements - 13434

the two curves  $\Gamma_1$  and  $\Gamma_2$ , cf. (5). The notch is at an angle of  $60^\circ$  and has a rounded tip with a radius of 1.3 mm. The left edge is fixed in  $y$ -direction and the top left corner node is fixed in both  $x$  and  $y$  direction. Displacement control on the right edge is used for this simulation with a displacement increment of  $\Delta \bar{\mathbf{w}} = 10^{-4}$  mm up to failure for phase-field simulations and  $\Delta \bar{\mathbf{w}} = 10^{-2}$  mm for shape optimization simulations. The material parameters are chosen as  $\lambda = 121.15$  GPa,  $\mu = 80.77$  GPa,  $G_c = 2.7$  N/mm. For the phase-field method, the length scale parameter was chosen as  $l_s = 0.01$  mm.

Figure 3 shows the comparison of the fracture paths between the phase-field and the shape optimization approach. On the left-hand side of the figure, blue represents the intact material and red represents the fractured regions. On the right-hand side, the curves representing the fracture are shown in red. From the results it can be seen that the crack paths from both approaches are in good

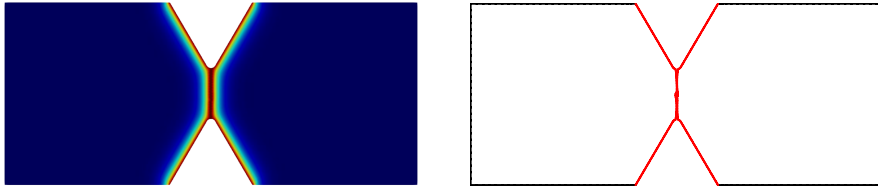


Figure 3: Fracture evolution results: phase-field (left) and shape optimization (right).

agreement.

## 4.2 Boundary Value Problem 2: Single-edge notch test – Anisotropy

We now model the single-edge notch test (SENT) for testing and validating the extension of the shape optimization approach towards anisotropic elastic media, e.g., monocrystals with a predefined orientation angle. For this numerical experiment we used a square plate with a width and height of 1 mm and a pre-existing crack from the left edge until the middle of the plate. The computational mesh consists of 69 014 elements and it is refined in the middle section where the crack is expected to develop, as shown in Figure 4. Furthermore, the curve representing the crack is again shown in red and has a width of  $2 \cdot 10^{-3}$  mm on the left edge of the domain (cf. Figure 1).

The elastic material stiffness matrix  $\mathbf{C}^{ref}$  (in VOIGT notation) for the reference coordinate system is defined as

$$\mathbf{C}^{ref} = \begin{pmatrix} 65 & 20 & 0 \\ 20 & 260 & 0 \\ 0 & 0 & 30 \end{pmatrix} \text{ GPa.}$$

Following [40], the critical energy is considered independent of the orientation angle and is taken as  $G_c = 1 \text{ N/mm}$ . For the phase-field simulations, the length scale parameter is chosen as  $l_s = 0.005 \text{ mm}$ . Simulations are performed using displacement control with an increment of  $\Delta \bar{\mathbf{w}} = 2 \cdot 10^{-5} \text{ mm}$  on the top edge when using the phase-field and  $\Delta \bar{\mathbf{w}} = 10^{-4} \text{ mm}$  when using the shape optimization approach. Further, we impose a homogenous DIRICHLET boundary condition in  $x$  direction on all nodes on the bottom edge and fix the bottom left corner of the domain in both  $x$  and  $y$  direction. Numerical computations are performed for brittle fracture with different anisotropy angles  $0^\circ$ ,  $30^\circ$ ,  $60^\circ$  and  $90^\circ$  measured from the horizontal axis.

The fracture paths for all anisotropy angles are depicted in Figure 5. We observe good qualitative agreement of the phase-field and the shape optimization approach, as the direction of fracture propagation between the two approaches is identical. The boundary forces for the phase-field simulations are shown in Figure 6 and for the shape optimization simulations in Figure 7. Also here, we

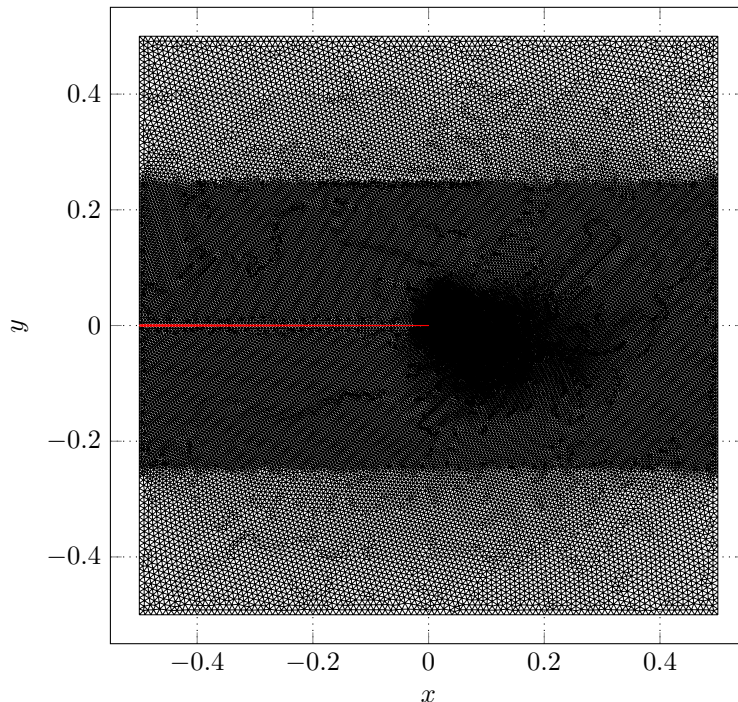


Figure 4: Mesh for SENT: Nodes - 34863, Elements - 69014

observe good qualitative agreement. However, the displacements at which the fracture initiates is lower in the phase field approach. This can be accounted to the lower stresses in the region of fracture due to the degradation function  $g(d)$ , cf. (11), and to the higher observed values of  $E_{frac}$  in both cases, before and after fracture propagation<sup>6</sup>, which are presented in Figure 8 and Figure 9 for both approaches.

## 5 Summary and conclusion

We have outlined a commonly-used model for crack propagation and described how this model is adapted to a phase-field method and to a novel approach for the simulation of crack propagation based on shape optimization techniques. Here, the crack is interpreted as (possibly multiple) piecewise open curves which are then used as the argument of a minimization problem. We have employed gradient descent techniques on a shape space admitting an infinite dimensional RIEMANNIAN manifold structure. This yields a mesh-independent approach and there is no requirement of staggered iterations. We have presented the numerical

<sup>6</sup>From (2) it can be seen that  $E_{frac} = 0.5 \text{ N mm}$  before and  $E_{frac} = 1 \text{ N mm}$  after crack propagation is expected for a fully horizontal crack path with  $G_c = 1 \text{ N/mm}$ .

implementation of both, the phase-field and shape optimization approach, and applied them to two benchmark cases. We have analyzed the results and see good agreement for the fracture path in the first benchmark case with isotropic material behavior. Numerical results for second benchmark case are generated for anisotropic material behavior. More extensive analyses are performed for different anisotropy angles and also show identical directions of fracture between the two different approaches. Further, the boundary forces are compared and show some differences with respect to the displacement at which fracture initiates, which are then discussed.

## Acknowledgements

This research work is funded by the projects ‘Structural Health Monitoring’ and ‘KIBIDZ – Intelligente Brandgefahrenanalyse für Gebäude und Schutz der Rettungskräfte durch Künstliche Intelligenz und Digitale Brandgebäudezwillinge’. Moreover, ‘hpc.bw’ also provides computational resources (HPC cluster HSU-per). All three projects are funded by dtec.bw – Digitalization and Technology Research Center of the Bundeswehr. dtec.bw is funded by the European Union – NextGenerationEU.

## Disclosure statement

The authors report there are no competing interests to declare.

## References

- [1] F. Aldakheel, B. Hudobivnik, A. Hussein, and P. Wriggers. Phase-field modeling of brittle fracture using an efficient virtual element scheme. *Computer Methods in Applied Mechanics and Engineering*, 341:443–466, 2018.
- [2] Fadi Aldakheel, Chaitanya Kandekar, Boris Benschmann, Hüsni Dal, and Richard Hanke-Rauschenbach. Electro-chemo-mechanical induced fracture modeling in proton exchange membrane water electrolysis for sustainable hydrogen production. *Computer Methods in Applied Mechanics and Engineering*, 400:115580, oct 2022. doi:10.1016/j.cma.2022.115580.
- [3] Fadi Aldakheel, Nima Noii, Thomas Wick, Olivier Allix, and Peter Wriggers. Multilevel global–local techniques for adaptive ductile phase-field fracture. *Computer Methods in Applied Mechanics and Engineering*, 387:114175, dec 2021. doi:10.1016/j.cma.2021.114175.
- [4] R. Alessi, M. Ambati, T. Gerasimov, S. Vidoli, and L. De Lorenzis. *Comparison of Phase-Field Models of Fracture Coupled with Plasticity*, pages 1–21. *Advances in Computational Plasticity 46*, Springer International Publishing, 2018.

- [5] G. Allaire, F. Jouve, and A.M. Toader. Structural optimization using sensitivity analysis and a level-set method. *Journal of Computational Physics*, 194(1):363–393, 2004. doi:10.1016/j.jcp.2003.09.032.
- [6] M. Ambati, T. Gerasimov, and L. De Lorenzis. Phase-field modeling of ductile fracture. *Computational Mechanics*, 55:1017–1040, 2015.
- [7] Marreddy Ambati, Tymofiy Gerasimov, and Laura De Lorenzis. A review on phase-field models of brittle fracture and a new fast hybrid formulation. *Computational Mechanics*, 55(2):383–405, 2015.
- [8] T. Bäck. *Evolutionary Algorithms in Theory and Practice. Evolution Strategies, Evolutionary Programming, Genetic Algorithms*. Oxford University Press, Oxford, 1996.
- [9] Klaus-Jürgen Bathe. *Finite Element Procedures*. Klaus-Jürgen Bathe, 2007.
- [10] Martin Berggren. A unified discrete–continuous sensitivity analysis method for shape optimization. *Computational Methods in Applied Sciences*, pages 25–39, 10 2009. doi:10.1007/978-90-481-3239-3\_4.
- [11] Jeremy Bleyer and Roberto Alessi. Phase-field modeling of anisotropic brittle fracture including several damage mechanisms. *Computer Methods in Applied Mechanics and Engineering*, 2018. <https://doi.org/10.1016/j.cma.2018.03.012>.
- [12] M. J. Borden, T. J. R. Hughes, C. M. Landis, and C. V. Verhoosel. A higher-order phase-field model for brittle fracture: Formulation and analysis within the isogeometric analysis framework. *Computer Methods in Applied Mechanics and Engineering*, 273:100–118, 2014.
- [13] B. L. Boyce et al. The second sandia fracture challenge: predictions of ductile failure under quasi-static and moderate-rate dynamic loading. *International Journal of Fracture*, 198(1-2):5–100, mar 2016. doi:10.1007/s10704-016-0089-7.
- [14] Chuanjie Cui, Rujin Ma, and Emilio Martínez-Pañeda. A phase field formulation for dissolution-driven stress corrosion cracking. *Journal of the Mechanics and Physics of Solids*, 147:104254, feb 2021.
- [15] Chuanjie Cui, Rujin Ma, and Emilio Martínez-Pañeda. A generalised, multi-phase-field theory for dissolution-driven stress corrosion cracking and hydrogen embrittlement. *Journal of the Mechanics and Physics of Solids*, 166:104951, sep 2022. doi:10.1016/j.jmps.2022.104951.
- [16] M. Droske and M. Rumpf. Multiscale joint segmentation and registration of image morphology. *IEEE Transactions on Pattern Analysis and Machine Intelligence*, 29(12):2181–2194, 2007.



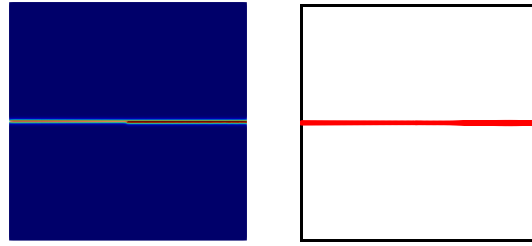
- [17] G.A. Francfort and J.-J. Marigo. Revisiting brittle fracture as an energy minimization problem. *J. Mech. Phys. Solids*, 46(8):1319–1342, 1998. doi:10.1016/S0022-5096(98)00034-9.
- [18] Caroline Geiersbach, Tim Suchan, and Kathrin Welker. Optimization of piecewise smooth shapes under uncertainty using the example of Navier-Stokes flow, 2023. doi:10.48550/ARXIV.2308.07742.
- [19] A.A. Griffith. The phenomena of rupture and flow in solids. *Philos. Trans. R. Soc. Lond.*, 221:163–198, 1921. doi:10.1098/rsta.1921.0006.
- [20] Michael Hintermüller and Wolfgang Ring. A second order shape optimization approach for image segmentation. *SIAM Journal on Applied Mathematics*, 64(2):442–467, jan 2004. doi:10.1137/s0036139902403901.
- [21] Hirshikesh, Sundararajan Natarajan, Ratna K. Annabattula, and Emilio Martínez-Pañeda. Phase field modelling of crack propagation in functionally graded materials. *Composites Part B: Engineering*, 169:239–248, 2019. doi:10.1016/j.compositesb.2019.04.003.
- [22] Daniel Höche, Wolfgang E. Weber, Eugen Gazenbiller, Sarkis Gavras, Norbert Hort, and Hajo Dieringa. Novel magnesium based materials: Are they reliable drone construction materials? a mini review. *Frontiers in Materials*, 8, apr 2021. doi:10.3389/fmats.2021.575530.
- [23] E. G. Kakouris and S. P. Triantafyllou. Phase-field material point method for brittle fracture. *International Journal for Numerical Methods in Engineering*, 112(12):1750–1776, 2017.
- [24] Chaitanya Kandekar, Aravinth Ravikumar, Daniel Höche, and Wolfgang E. Weber. A partitioned computational framework for damage evolution in stress corrosion cracking utilizing phase-field. *PAMM*, 22(1):e202200211, 2023. doi:10.1002/pamm.202200211.
- [25] C.S. Kappelos, E.M. Papoutsis-Kiachagias, K.C. Giannakoglou, and M. Hartmann. The unsteady continuous adjoint method for minimizing flow-induced sound radiation. *Journal of Computational Physics*, 392:368–384, 2019.
- [26] D.G. Kendall. Shape manifolds, procrustean metrics, and complex projective spaces. *Bulletin of the London Mathematical Society*, 16(2):81–121, 03 1984. doi:10.1112/blms/16.2.81.
- [27] Charlotte Kuhn and Ralf Müller. A continuum phase field model for fracture. *Engineering Fracture Mechanics*, 77(18):3625 – 3634, 2010.
- [28] Charlotte Kuhn, Alexander Schlüter, and Ralf Müller. On degradation functions in phase field fracture models. *Computational Materials Science*, 108:374 – 384, 2015.

- [29] Bin Li, Christian Peco, Daniel Millán, Irene Arias, and Marino Arroyo. Phase-field modeling and simulation of fracture in brittle materials with strongly anisotropic surface energy. *International Journal for Numerical Methods in Engineering*, 102(3-4):711–727, jul 2014. doi:10.1002/nme.4726.
- [30] H. Ling and D.W. Jacobs. Shape classification using the inner-distance. *IEEE Transactions on Pattern Analysis and Machine Intelligence*, 29(2):286–299, 2007.
- [31] R. Löhner, O. Soto, and C. Yang. An adjoint-based design methodology for CFD optimization problems. In *41st Aerospace Sciences Meeting and Exhibit, Reno, Nevada*, page 299, 2003.
- [32] Weijie Mai, Soheil Soghrati, and Rudolph G. Buchheit. A phase field model for simulating the pitting corrosion. *Corrosion Science*, 110:157–166, sep 2016. doi:10.1016/j.corsci.2016.04.001.
- [33] P. W. Michor and D. Mumford. An overview of the Riemannian metrics on spaces of curves using the Hamiltonian approach. *Applied and Computational Harmonic Analysis*, 23(1):74–113, July 2007. doi:10.1016/j.acha.2006.07.004.
- [34] P.W. Michor and M. Mumford. Riemannian geometries on spaces of plane curves. *Journal of the European Mathematical Society (JEMS)*, 8(1):1–48, 2006. doi:10.4171/JEMS/37.
- [35] C. Miehe, F. Welschinger, and M. Hofacker. Thermodynamically consistent phase-field models of fracture: Variational principles and multi-field FE implementations. *International Journal for Numerical Methods in Engineering*, 83:1273–1311, 2010.
- [36] Christian Miehe, Martina Hofacker, and Fabian Welschinger. A phase field model for rate-independent crack propagation: Robust algorithmic implementation based on operator splits. *Computer Methods in Applied Mechanics and Engineering*, 199(45):2765–2778, 2010. URL: <https://www.sciencedirect.com/science/article/pii/S0045782510001283>, doi:10.1016/j.cma.2010.04.011.
- [37] J. Mikota, H. Reiter, and Wolfgang E. Weber. Development of a compact and zunable vibration compensator for hydraulic systems. *International Journal of Fluid Power*, 04(1), 2003. doi:<https://journals.riverpublishers.com/index.php/IJFP/article/view/612>.
- [38] W. Mio, A. Srivastava, and S. Joshi. On shape of plane elastic curves. *International Journal of Computer Vision*, 73(3):307–324, September 2006. doi:10.1007/s11263-006-9968-0.

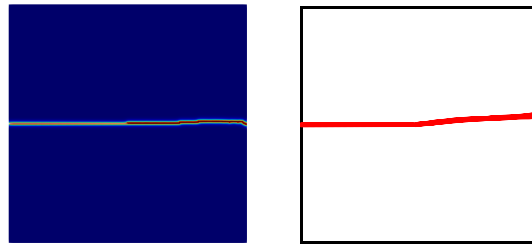
- [39] Thanh-Tung Nguyen, Julien Réthoré, Julien Yvonnet, and Marie-Christine Baietto. Multi-phase-field modeling of anisotropic crack propagation for polycrystalline materials. *Computational Mechanics*, 60(2):289–314, apr 2017. doi:10.1007/s00466-017-1409-0.
- [40] Thanh-Tung Nguyen, Julien Yvonnet, Danièle Waldmann, and Qi-Chang He. Implementation of a new strain split to model unilateral contact within the phase field method. *International Journal for Numerical Methods in Engineering*, 121(21):4717–4733, aug 2020. doi:10.1002/nme.6463.
- [41] Arne Nägel, Volker Schulz, Martin Siebenborn, and Gabriel Wittum. Scalable shape optimization methods for structured inverse modeling in 3d diffusive processes. *Computing and Visualization in Science*, 17(2):79–88, apr 2015. doi:10.1007/s00791-015-0248-9.
- [42] C. Othmer. A continuous adjoint formulation for the computation of topological and surface sensitivities of ducted flows. *International Journal for Numerical Methods in Fluids*, 58(8):861–877, 2008. doi:10.1002/flid.1770.
- [43] Lidiya Pryymak, Tim Suchan, and Kathrin Welker. A product shape manifold approach for optimizing piecewise-smooth shapes. In Frank Nielsen and Frédéric Barbaresco, editors, *Geometric Science of Information. GSI 2023*, volume 14071 of *Lecture Notes in Computer Science*, pages 21–30, Cham, 2023. Springer Nature Switzerland. doi:10.1007/978-3-031-38271-0\_3.
- [44] Lars Radtke, Georgios Bletsos, Niklas Kühn, Tim Suchan, Thomas Rung, Alexander Düster, and Kathrin Welker. Parameter-free shape optimization: various shape updates for engineering applications. *Aerospace*, 10(751), 2023. doi:10.3390/aerospace10090751.
- [45] Natalie Rauter and Wolfgang E. Weber. On the influence of the probabilistic microstructural characteristics of glass fiber-reinforced composites on the wave propagation in GLARE. *PAMM*, 23(1), may 2023. doi:10.1002/pamm.202200132.
- [46] Max Rottmann, Thomas Roloff, Natalie Rauter, Liv Rittmeier, Michael Sinapius, and Wolfgang E. Weber. A numerical study on planar gradient acoustic impedance matching for guided ultrasonic wave detection. *Journal of Vibration and Control*, page 107754632211497, jan 2023. doi:10.1177/10775463221149764.
- [47] M. Rumpf and B. Wirth. A nonlinear elastic shape averaging approach. *SIAM Journal on Imaging Sciences*, 2(3):800–833, 2009.
- [48] S. Schmidt, E. Wadbro, and M. Berggren. Large-scale three-dimensional acoustic horn optimization. *SIAM Journal on Scientific Computing*, 38(6):B917–B940, 2016. doi:10.1137/15M1021131.

- [49] Stephan Schmidt. Weak and strong form shape Hessians and their automatic generation. *SIAM Journal on Scientific Computing*, 40(2):C210–C233, Jan 2018. doi:10.1137/16m1099972.
- [50] Volker H. Schulz. A Riemannian view on shape optimization. *Foundations of Computational Mathematics*, 14(3):483–501, April 2014. doi:10.1007/s10208-014-9200-5.
- [51] Volker H. Schulz, Martin Siebenborn, and Kathrin Welker. Efficient PDE constrained shape optimization based on Steklov-Poincaré-type metrics. *SIAM Journal on Optimization*, 26(4):2800–2819, 2016. doi:10.1137/15m1029369.
- [52] M. Siebenborn and K. Welker. Algorithmic aspects of multigrid methods for optimization in shape spaces. *SIAM Journal on Scientific Computing*, 39(6):B1156–B1177, 2017. doi:10.1137/16M1104561.
- [53] N. Singh, C.V. Verhoosel, R. de Borst, and E.H. van Brummelen. A fracture-controlled path-following technique for phase-field modeling of brittle fracture. *Finite Elements in Analysis and Design*, 113:14 – 29, 2016.
- [54] Orlando Soto and Rainald Löhner. *On the Boundary Computation of Flow Sensitivities*, pages 1–11. American Institute of Aeronautics and Astronautics, 2004. doi:10.2514/6.2004-112.
- [55] Tim Suchan, Kathrin Welker, and Winnifried Wollner. A new shape optimization approach for fracture propagation. *Proceedings in Applied Mathematics and Mechanics*, 22(1):e202200124, 2023. doi:10.1002/pamm.202200124.
- [56] S. Teichtmeister, D. Kienle, F. Aldakheel, and M.-A. Keip. Phase field modeling of fracture in anisotropic brittle solids. *International Journal of Non-Linear Mechanics*, 97:1–21, 2017.
- [57] B.D. Upadhyay, S.S. Sonigra, and S.D. Daxini. Numerical analysis perspective in structural shape optimization: A review post 2000. *Advances in Engineering Software*, 155:102992, 2021. URL: <https://www.sciencedirect.com/science/article/pii/S0965997821000211>, doi:10.1016/j.advengsoft.2021.102992.
- [58] Woldemar Voigt. *Lehrbuch der Kristallphysik (Mit Ausschluss der Kristallographie)*, volume 34. BG Teubner, 1910.
- [59] B. Wirth, L. Bar, M. Rumpf, and G. Sapiro. A continuum mechanical approach to geodesics in shape space. *International Journal of Computer Vision*, 93(3):293–318, 2010.
- [60] Peter Wriggers. *Nonlinear Finite Element Methods*. Springer Berlin Heidelberg, 2008. doi:10.1007/978-3-540-71001-1.

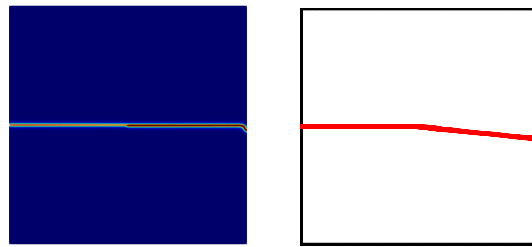
- [61] Xue Zhang, Chet Vignes, Scott W. Sloan, and Daichao Sheng. Numerical evaluation of the phase-field model for brittle fracture with emphasis on the length scale. *Computational Mechanics*, 59(5):737–752, 2017.
- [62] J.-P. Zolésio. Control of moving domains, shape stabilization and variational tube formulations. In K. Kunisch, J. Sprekels, G. Leugering, and F. Tröltzsch, editors, *International Series of Numerical Mathematics*, pages 329–382. Birkhäuser Basel, 2007. doi:10.1007/978-3-7643-7721-2\_15.



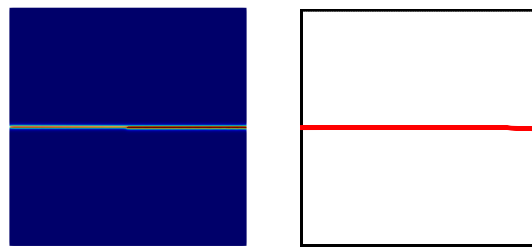
(a)  $\theta = 0^\circ$



(b)  $\theta = 30^\circ$



(c)  $\theta = 60^\circ$



(d)  $\theta = 90^\circ$

Figure 5: Fracture paths for different angles  $\theta$  of the anisotropic material.

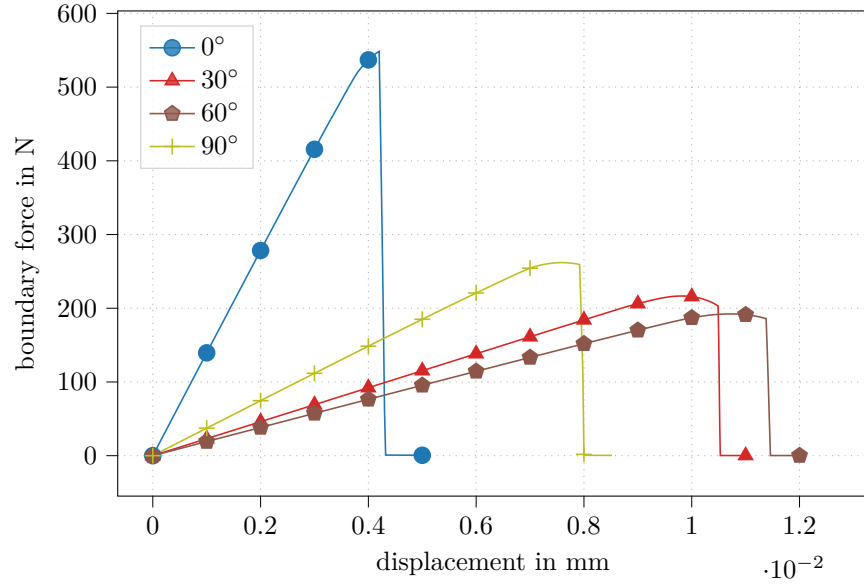


Figure 6: Boundary force for SENT anisotropy with the phase-field approach.

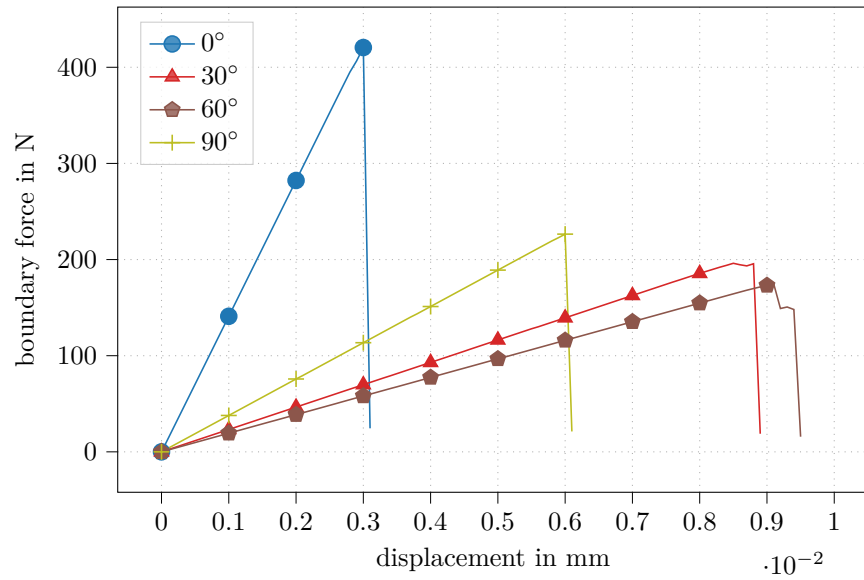


Figure 7: Boundary force for SENT anisotropy with the shape optimization approach.

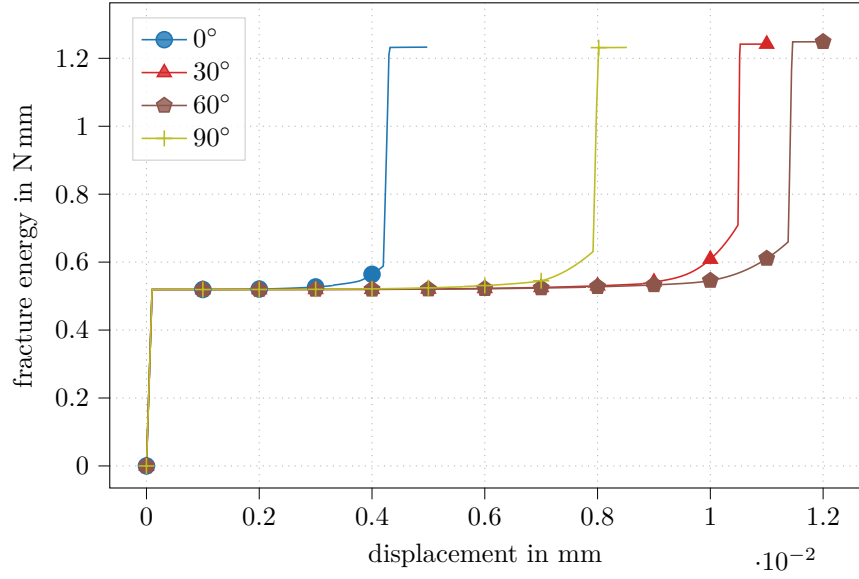


Figure 8: Fracture energy for SENT anisotropy with the phase-field approach.

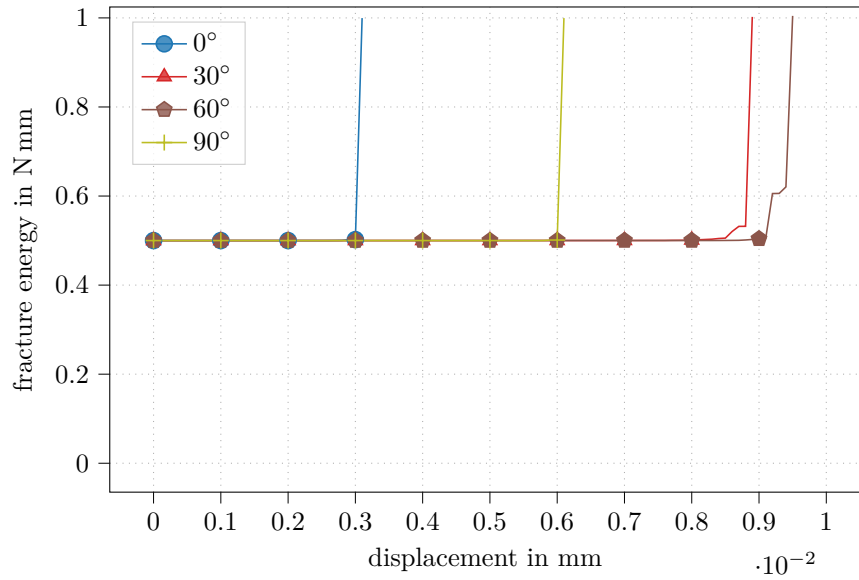


Figure 9: Fracture energy for SENT anisotropy with the shape optimization approach.